Available online at www.sciencedirect.com
ScienceDirect
International Journal of Heat and Mass Transfer 50 (2007) 4052–4062
International Journal of HEAT and MASS TRANSFER
www.elsevier.com/locate/ijhmt

Effect of variable permeability porous medium inter-connectors on the thermo-hydraulics of heat exchanger modelled as porous media

Arunn Narasimhan *, K. Sumithra Raju [1]

Heat Transfer and Thermal Power Laboratory, Department of Mechanical Engineering, Indian Institute of Technology Madras, Chennai, Tamil Nadu 600036, India

Received 24 October 2006; received in revised form 2 January 2007
Available online 26 April 2007

Abstract

Using numerical methods, the effect of spatially variable permeability of porous medium tube-to-tube inter-connectors on the thermo-hydraulics of near-compact heat exchangers (NCHX, surface to volume ratio, $\alpha = 100$–$300\ m^2/m^3$), is studied. The porous medium connects the tubes ($D = 2$ mm) of the NCHX kept in in-line arrangement along the flow direction having a square pitch of $X_T = X_L = 2.25$. This novel study further treats the NCHX itself as a global porous medium characterized with global permeability (K_g) and form coefficient (C_g), which is being influenced by the local tube-to-tube inter-connector porous medium, characterized with a local permeability (K_i). The cooling fluid with $Pr = 0.7$ is under laminar flow ($10 < Re < 100$) through the NCHX with and without local PM inter-connectors of uniform permeability (UP, PMC1 and PMC2 with $K_i = 10^{-5}$ and $10^{-10}\ m^2$, respectively) and variable permeability (VP, PMC3 and PMC4 with K_i varying along the flow direction from 10^{-5} to $10^{-10}\ m^2$ and 10^{-10} to $10^{-05}\ m^2$, respectively). At higher flow rates ($Re > 70$) it is shown that PMC4 registers less pressure-drop compared to PMC1, the UP case with highest K_i. Nusselt number variation for Re for VP cases (PMC3 and PMC4) is bounded by the two limiting UP cases PMC1 and PMC2, for identical porosity. Comparisons between NCHX tube bank in the UP and VP cases are done using an overall enhancement ratio (ER), which was found to increase with increasing K_i of the PM inter-connectors. Treating the NCHX models as a global porous medium, two useful engineering correlations are presented to predict the ξ and Nu as a function of Re and the non-dimensional global porous medium drag coefficients Da_g and Du_g (which are functions of local K_i). Both correlations predict the numerical data with $\pm 6\%$ accuracy within the range of Re tested.

Keywords: Porous medium; Variable permeability; Tube banks; Compact heat exchangers; Metal foams; Heat transfer enhancement

1. Introduction

Heat transfer enhancement in forced convection configuration using porous medium (PM), in particular, with variable properties (permeability and porosity), is a sought after technique [1–4] in industrial applications like heat exchangers [2,3] and electronics cooling heat sinks [5–8]. For instance, the effect of variable permeability of PM in the transverse direction on Nu is reviewed recently [4] using analytical solutions and it is found that the increase in Nu is due to the variation in transverse permeability (K, m^2). In typical forced convection applications such as flow through channels with discrete heat sources [9,10], the usage of PM with uniform properties imposes higher pumping power and even less heat removal in the gaps between the heat sources, as the axial distance increases. To achieve less pumping power without sacrificing heat transfer enhancement, a possible way is to use PM with spatially varying properties (permeability and porosity) and/or to use PM in partly filled forced convection configurations.

Use of PM with spatially varying permeability (VP), for instance, resulted [11] in considerably altered local velocity field for combined free and forced convection from an inclined vertical surface saturated with porous medium.

* Corresponding author. Tel.: +91 44 22574696; fax: +91 44 225 78501.
E-mail address: arunn@iitm.ac.in (A. Narasimhan).
[1] Ph.D student.

0017-9310/$ - see front matter © 2007 Elsevier Ltd. All rights reserved.
doi:10.1016/j.ijheatmasstransfer.2007.01.058

Nomenclature

A	surface area of the tube, (πD), m^2
A_1	minimum cross sectional area between tube to tube, m^2
C	form coefficient, m^{-1}
c_p	specific heat, J kg^{-1} K^{-1}
CF	clear fluid domain
D	diameter of the tube, m
Da	Darcy number, (K$^{0.5}$/D)
Du	Dupuit number, (CD)
ER	enhancement ratio, Eq. (25)
Eu	Euler number, ($p_{in} - p/\rho U^2$)
k	thermal conductivity, W m^{-1} K^{-1}
K	permeability, m^2
L	length of the tube bank, m
L_B	length of the buffer zone, m
$\dot{m}$	mass flow rate, kg/s, Eq. (24)
NCHX	near compact heat exchangers
Nu	average Nusselt number, Eq. (22)
p	pressure, Pa
PM	porous medium, Fig. 1
PMC	porous medium case
Pr_e	effective Prandtl number ($\nu/k_e/(\rho c_p)_f$)
ΔP	global longitudinal pressure-drop across the tube bank
q	total heat transfer, W
R	overall energy gain, Eq. (24)
Re_D	Reynolds number, ($U_m D/\nu$)
S_L	longitudinal tube pitch, m, Fig. 1
S_T	transverse tube pitch, m, Fig. 1
T_w	wall temperature, K
T_b	bulk mean temperature, K
T_∞	free-stream temperature, K, Fig. 1
u	x-direction local and seepage speed in CF and PM zones, m s^{-1}, Fig. 1
UP	inter-connectors with uniform permeability configuration
U	dimensionless velocity, (u/U_∞)
U_∞	free-stream velocity, m s^{-1}
U_m	average velocity at minimum cross section, m s^{-1}, Fig. 1
v	y-direction local and seepage speed in CF and PM zones, m s^{-1}, Fig. 1
VP	inter-connectors with variable permeability configuration
X	dimensionless distance in x-direction, (x/D)
X_L	dimensionless longitudinal tube pitch, S_L/D, Fig. 1
X_T	dimensionless transverse tube pitch, S_T/D, Fig. 1
Y	dimensionless distance in y-direction, (y/D)

Greek symbols

α	thermal diffusivity, (m^2 s^{-1})
τ	dimensionless transverse thickness of inter-connector porous medium, t/S$_n$, Fig. 1
ϕ	porosity of the interconnecting PM
λ	constants (take values 1 or 0) used to flag terms in Eqs. (2),(3) and (7),(8)
θ	dimensionless temperature, $((T - T_{in})/(T_w - T_{in}))$
μ	dynamic viscosity, N s m^{-2}
ν	kinematic viscosity, m^2 s^{-1}
ρ	density, kg m^{-3}
ξ	non-dimensional pressure-drop, Eq. (15)

Subscripts

b	bulk
c	cross section
e	effective
f	fluid
g	global porous medium
i	inter-connector porous medium
n	normal, local
s	solid

Free convection investigation [12] from inclined permeable wall embedded in a variable permeability PM resulted again in the sharp increase in local velocity profile due to PM with VP, leading to enhanced heat transfer compared to the uniform permeability (UP) case.

On the other hand, even in the UP case, use of partially filled PM configuration can still result in enhanced heat transfer with less pumping power as reported for instance in [13], where heat transfer enhancement in channel is achieved using partially filled PM inserts. More recent numerical investigations [14] reveal that partially filled porous medium configuration of about 60% of channel height enhances heat transfer rate in a heat exchanger under laminar flow of air. It was also reported that the form-drag term is found to be not important when $Da < 10^{-4}$, for the PM used. Entropy generation in pipes and channels partially filled with PM simulating the fouling effect in heat exchangers has also been investigated [15]. A recent review chapter [16] has collected other earlier analytical research contributions in this direction and has also discussed the proper interface boundary conditions to be used in partly filled PM configuration.

The idea proposed in this paper combines these two options of partly filled PM configuration and variable permeability PM configuration, to use metal foam type PM with spatially variable permeability ($10^{-5} < K < 10^{-10}$, m^2) as tube-to-tube inter-connectors in a cross flow, *near*-compact heat exchanger, NCHX, ($\alpha = 100$–300 m^2/m^3) with inline arrangement of tubes ($d = 2$ mm). The local PM inter-connectors are of the size of the tube diameter

and hence the NCHX configuration can be modelled as a partly filled global PM configuration of spatially variable permeability.

2. Model description and boundary conditions

Fig. 1a displays the schematic of the NCHX with aligned tubes with PM inter-connectors arrangement, under cross flow. The PM inter-connectors with transverse thickness (t, m) equal to that of the NCHX tube diameter ($D = 2$ mm), are employed only in the longitudinal direction (Fig. 1b). The governing equations of mass, momentum and energy balance used in this study are

$$\frac{\partial u}{\partial x}+\frac{\partial v}{\partial y}=0 \tag{1}$$

$$\rho\left(u\frac{\partial u}{\partial x}+v\frac{\partial u}{\partial y}\right)=-\frac{\partial p}{\partial x}+\lambda_1\mu\left(\frac{\partial^2 u}{\partial x^2}+\frac{\partial^2 u}{\partial y^2}\right)+\lambda_2\frac{\mu}{K}u \tag{2}$$

$$\rho\left(u\frac{\partial v}{\partial x}+v\frac{\partial v}{\partial y}\right)=-\frac{\partial p}{\partial y}+\lambda_1\mu\left(\frac{\partial^2 v}{\partial x^2}+\frac{\partial^2 v}{\partial y^2}\right)+\lambda_2\frac{\mu}{K}v \tag{3}$$

$$\rho c_p\left(u\frac{\partial T}{\partial x}+v\frac{\partial T}{\partial y}\right)=k_e\left(\frac{\partial^2 T}{\partial x^2}+\frac{\partial^2 T}{\partial y^2}\right). \tag{4}$$

Using the dimensionless variables, namely,

$$U=u/U_\infty;\quad V=v/U_\infty;\quad X=x/D;\quad Y=y/D;$$
$$\theta=T-T_{\text{in}}/T_{\text{w}}-T_{\text{in}};\quad P=p/\rho U_\infty^2 \tag{5}$$

the dimensionless form of the above governing equations can be obtained as follows

$$\frac{\partial U}{\partial X}+\frac{\partial V}{\partial Y}=0 \tag{6}$$

$$\left(U\frac{\partial U}{\partial X}+V\frac{\partial U}{\partial Y}\right)=-\frac{\partial P}{\partial X}+\frac{\lambda_1}{Re_D}\left(\frac{\partial^2 U}{\partial X^2}+\frac{\partial^2 U}{\partial Y^2}\right)+\lambda_2\frac{U}{Re_D Da^2} \tag{7}$$

$$\left(U\frac{\partial V}{\partial X}+V\frac{\partial V}{\partial Y}\right)=-\frac{\partial P}{\partial Y}+\frac{\lambda_1}{Re_D}\left(\frac{\partial^2 V}{\partial X^2}+\frac{\partial^2 V}{\partial Y^2}\right)+\lambda_2\frac{V}{Re_D Da^2} \tag{8}$$

$$\left(U\frac{\partial \theta}{\partial X}+V\frac{\partial \theta}{\partial Y}\right)=\frac{1}{Pr_e Re_D}\left(\frac{\partial^2 \theta}{\partial X^2}+\frac{\partial^2 \theta}{\partial Y^2}\right). \tag{9}$$

The above conservation equations are solved in the domain of Fig. 1, for both clear (of porous medium) fluid flow and porous medium flow by setting the parameters λ_1 and λ_2 as unity and zero, respectively, in clear fluid zone and μ_{eff}/μ and unity, respectively, in the porous medium zone so that Eqs. (7) and (8) automatically satisfy the porous-fluid zone interface condition (see Fig. 1) detailed in the following section. The effective thermal conductivity used in Eq. (9) (represented in Pr_e) is calculated using the model $k_e=(1-\varphi)k_s+\varphi k_f$ (all the symbols are explained in the nomenclature).

The computational domain considered in the present problem (Fig. 1a) can be simplified using periodic boundary conditions [17]. However, the flow field in the present problem cannot be periodically thermally fully developed even though it could be hydro-dynamically fully developed. This is due to the presence of the porous medium, which results in a non-periodic diffusion dominated flow domain. However, owing to the symmetry of the domain, Fig. 1a, the flow through the tube bank can be simulated accurately by calculating the flow through the half section of one row in the direction of flow as shown in Fig. 1b. To complete the problem formulation, the following boundary conditions are used in location as shown in Fig. 1b.

No slip boundary condition is imposed at the tube wall by setting both components of velocity (U, V) to zero. Since the flow is laminar and steady, a symmetry condition can be imposed as shown in Fig. 1b, while at the inlet to the channel a known uniform velocity field is assumed. Since,

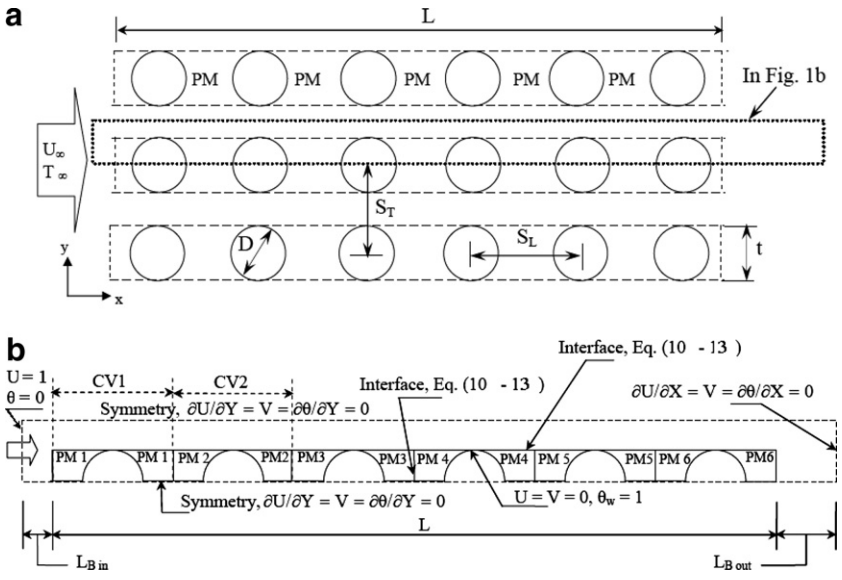

Fig. 1. (a) Schematic of the configuration (b) boundary conditions and computational domain.

Table 1
Local permeability values for each cylinder of four set of arrangements with same porosity

Case	Cylinder 1 (K, m^2)	Cylinder 2 (K, m^2)	Cylinder 3 (K, m^2)	Cylinder 4 (K, m^2)	Cylinder 5 (K, m^2)	Cylinder 6 (K, m^2)
PMC 1	4.44×10^{-05}	4.44×10^{-05}	4.44×10^{-05}	4.44×10^{-05}	4.44×10^{-05}	4.44×10^{-05}
PMC 2	4.44×10^{-10}	4.44×10^{-10}	4.44×10^{-10}	4.44×10^{-10}	4.44×10^{-10}	4.44×10^{-10}
PMC 3	4.44×10^{-05}	4.44×10^{-05}	4.44×10^{-05}	4.44×10^{-10}	4.44×10^{-10}	4.44×10^{-10}
PMC 4	4.44×10^{-10}	4.44×10^{-10}	4.44×10^{-10}	4.44×10^{-05}	4.44×10^{-05}	4.44×10^{-05}

the location of velocity inlet can affect the numerical solution of the given computational domain, sufficient buffer length has been provided at the inlet ($L_{\text{B-in}}$) such that flow should be uniform (U_∞, θ_∞) without thermal 'back' diffusion at the inlet. At the exit, fully-developed flow condition is imposed, a requirement met by an additional buffer length ($L_{\text{B-out}}$) provided at the exit between the last cylinder and the exit.

Two pairs of interface boundary conditions (a) between porous medium and clear fluid flow (b) between two interconnector porous media (see Fig. 1b), are required for solving the momentum and energy equations in the present study, in order to accommodate the discontinuity in the diffusion flux of momentum and energy, respectively. We adopt here, the boundary conditions proposed in [18] for partially filled porous medium configurations and verified in [4,16,18] for similar configurations, namely,

$$U_f|_{CF} = U_f|_{PM} \quad \text{and} \quad \mu_{eff}\left.\frac{dU_f}{dY}\right|_{PM} - \mu_f\left.\frac{dU_f}{dY}\right|_{CF} = \beta\frac{\mu_f}{Da}U_f|_{interface} \tag{10}$$

$$U_f|_{PMn} = U_f|_{PMn+1} \quad \text{and} \quad \mu_{eff}\left.\frac{dU_f}{dY}\right|_{PMn} - \mu_{eff}\left.\frac{dU_f}{dY}\right|_{PMn+1} = \beta\frac{\mu_f}{Da}U_f|_{interface} \tag{11}$$

$$\theta|_{CF} = \theta|_{PM} \quad \text{and} \quad k_{eff}\left.\frac{d\theta}{dY}\right|_{PM} = k_f\left.\frac{d\theta}{dY}\right|_{CF} \tag{12}$$

$$\theta|_{PMn} = \theta|_{PMn+1} \quad \text{and} \quad k_{eff}\left.\frac{d\theta}{dY}\right|_{PMn} = k_{eff}\left.\frac{d\theta}{dY}\right|_{PMn+1} \tag{13}$$

For the range of local permeability values used in this paper (Table 1), in Eqs. (10) and (11), β can be set as zero, as explained in [19], resulting in Eqs. (6) and (7) to retain their Brinkman extended Darcy differential formulation of the momentum statement inside the porous layer. This allows for continuity of velocity and shear stress at the fluid-porous layer interface and a no-slip condition at the solid wall. Similar explanation is consistent with the use of Eqs. (12) and (13) as the interface boundary conditions for solving the energy equation, Eq. (8).

3. Numerical procedure and validation

Using numerical methods the above problem was solved, employing the finite volume method to discretise the set of partial differential equations, Eqs. (5)–(8). Implicit, second order upwind solver is used with the velocity and pressure coupling achieved by the SIMPLE [20] algorithm. The convergence criterion (difference between the results of two successive iterations) for the continuity residual is set as 10^{-3}, momentum equation as 10^{-6} and for the energy equation as 10^{-9}. The grid independence study, using the various non-dimensional numbers which are calculated for four successive grid levels at $Re = 100$ for flow over a tube bank (Fig. 1), doubling the total grid points in each level. A suitable grid is chosen by checking for the error between two successive levels of grid refinement to be less than 1% for both the Eu and the Nu values. For the computation work reported in this study, a quadrilateral uniform grid in both x- and y-direction with 12,462 nodes is used over the numerical domain of Fig. 1b. Further details of the extensive validation and related graphs are available in [21,22].

4. Hydro-dynamic results

Fig. 2a and b shows at $Re = 10$, the effect of PM interconnectors 'local' permeability (aluminium metal foam of $k = 202$ W/m K) placed between the tubes with fixed transverse thickness ($\delta = D$), on the local dimensionless velocity profiles at mid-plane and exit of the configuration considered (see Fig. 1b). Similarly, Fig. 2c and d depict the velocity profiles at the mid-place and exit for $Re = 100$. In both situations of $Re = 10$ and 100 (Fig. a through d), the CF case ($K_i = K_{CF}$) and the UP case PMC1 with highest 'local' permeability ($K_i = 10^{-5}$ m^2, Table 1) offer little viscous resistance in the gaps between the cylinders, resulting in more local flow. This is compensated with the corresponding reduction in the local velocity near the axis, as mass conservation is imposed across the boundaries of the control volume. The PMC2 with lowest 'local' permeability ($K_i = 10^{-10}$ m^2, Table 1) provides the largest porous medium viscous frictional resistance to the flow in the gaps, where these PM inter-connectors are placed, and hence the local velocity is the lowest in the gaps and correspondingly, highest towards the axis. The velocity profiles for the PMC2 and PMC3, VP cases, fall in between the limits of PMC1 and PMC4.

It is interesting to observe from Fig. 2d (exit plane, $Re = 100$) that the local velocity profiles for the VP case with spatially varying permeability, PMC3 ($K_i = 10^{-5}$–10^{-10} m^2, Table 1), registers similar trend as that of PMC2 ($K_i = 10^{-10}$ m^2, Table 1), the UP case of lowest K_i, because of their similar geometry of local (K_i) inter-connectors across their last three cylinders. Similar reasoning can be made for the complementary effect of lowest local speed near the gaps between the cylinders and the corresponding maximum local speeds near the axis observed with VP case, PMC4 ($K_i = 10^{-10}$–10^{-5} m^2, Table 1). Both

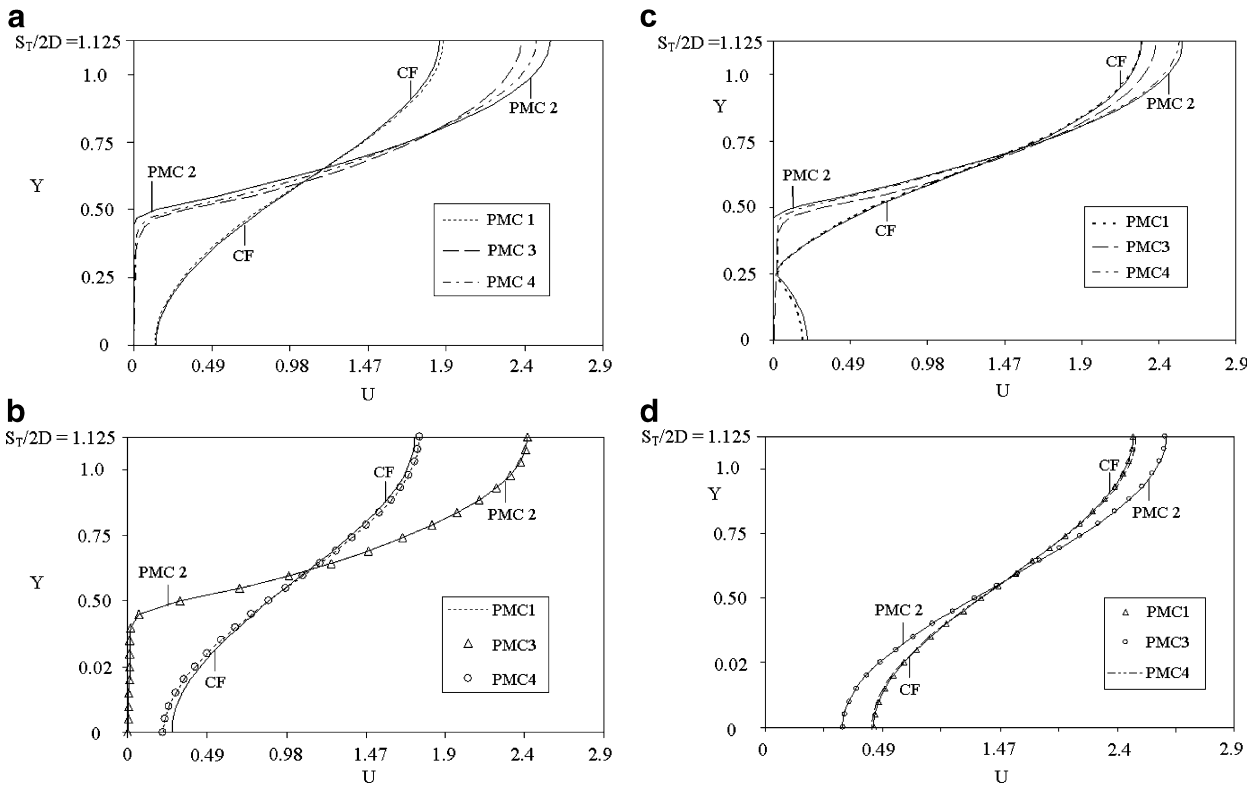

Fig. 2. Local dimensionless velocity U variation with Y for $Re = 10$ at (a) mid-section (b) exit and for $Re = 100$ at (c) mid-section (d) exit of the NCHX configuration.

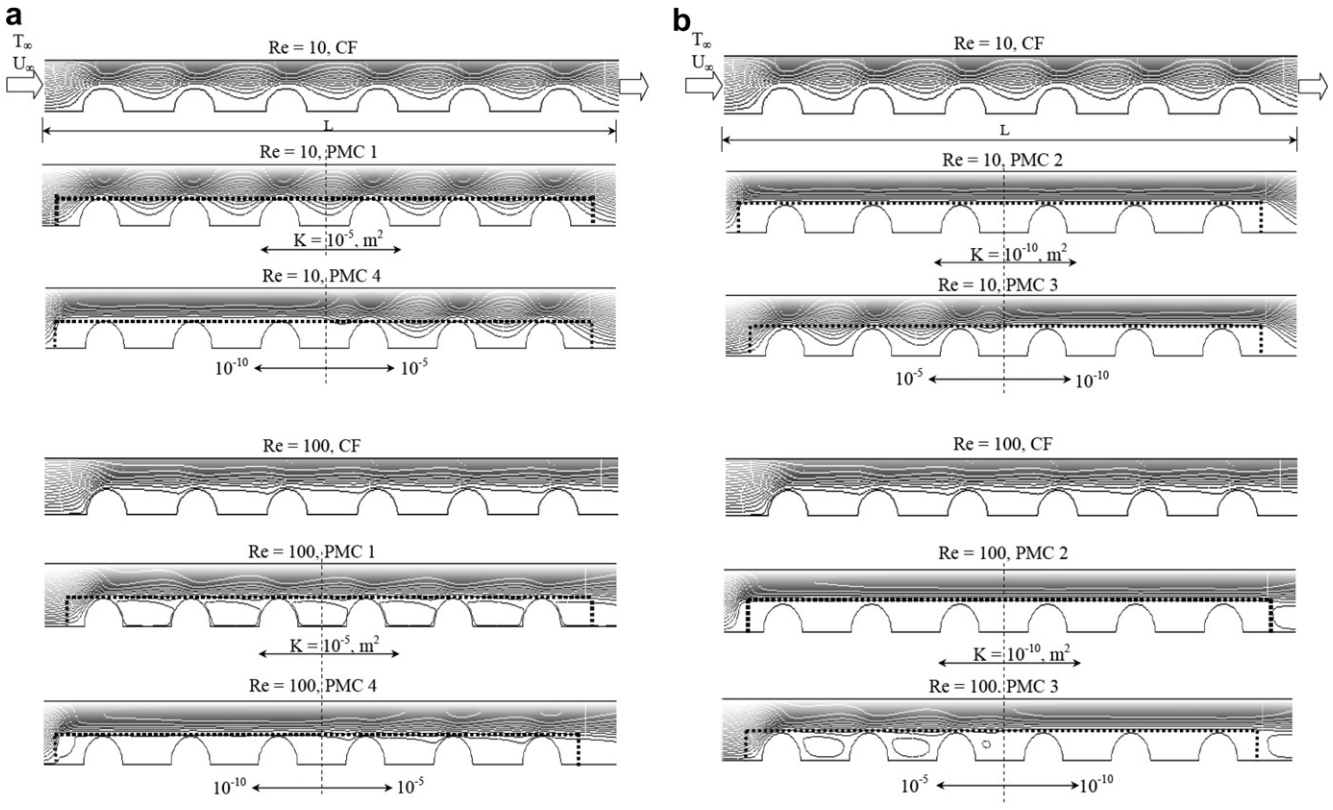

Fig. 3. Comparison of streamlines for the CF and PM configuration listed in Table 1, at $Re = 10$ and 100 (a) CF, PMC1 and PMC4 (b) CF, PMC2 and PMC3.

of these velocity profiles, due to their high local permeability, are similar to that of the CF case.

Fig. 3a and b illustrate the streamlines for $Re = 10$ and $Re = 100$, in the chosen computational domain with six cylinders (Fig. 1b) for the UP and the VP cases. The parallel nature of the inlet and exit streamlines in all the cases of Fig. 3a and b clearly substantiates the sufficiency of the buffer zone length (L_B) chosen at the entry and exit of the computational domain to meet the outflow and the velocity inlet boundary condition as discussed in the previous section. The similarity in the depth of penetration of the streamlines in the gaps between the last three cylinders of PMC1 and PMC4 at $Re = 100$ in Fig. 3a and of PMC2 and PMC3 in the corresponding Fig. 3b, corroborate the explanation for the nature of the local velocity profiles near the exit (Fig. 2a and b) given in the previous paragraph.

The NCHX configuration of Fig. 1 with the PM cases listed in Table 1, can be perceived as a 'global' porous medium [21,23], whose overall global pressure-drop is governed by the Hazen–Dupuit–Darcy relation [23] of the form

$$\frac{\Delta P}{L} = \frac{\mu}{K_g} U + \rho C_g U^2 \tag{14}$$

where K_g and C_g are the global permeability and form coefficient of the 'global' porous medium, respectively. These 'global' porous medium properties K_g and C_g can be obtained from the curve-fit results of Eq. (14) for the pressure-drop versus average fluid speed data, and are influenced by the properties ϕ and K_i of the inter-connector 'local' porous medium, PMC 1–4, listed in Table 1. The K_g and C_g thus found are listed in Table 2.

From the Table 2, it is interesting to observe the identical C_g values for the pairs, PMC1 and PMC3 and PMC2 and PMC4, respectively. If one were to perceive the PMC1 configuration as a 'global' porous medium, (2nd and 5th picture from the top, in both Fig. 3a and b), it is a porous medium allowing distributed flow all through its structure for the range of Re tested. This is because the gaps of the cylinders for PMC1 are connected by local PM with $K_i = 10^{-5}\,m^2$ (the highest permeability). This results in the flow to change its direction transversally more often, while it goes through PMC1. Since form drag is governed by the shape of the porous medium [24] the resultant flow accelerates or decelerates around the shape of the solid matrix, PMC1 imposes a higher form drag for the flow. This is reflected in the higher value of form coefficient for PMC1, as can be seen from Table 2. Similar result of flow structure can be observed for PMC3 also, (see 3rd and 6th picture of Fig. 3b) in the first three cylinders. The effect of the flow structure over the last three cylinders seems not to affect the form drag component at all, as seen from the identical C_g results for PMC1 and PMC3, both having the first three cylinders filled by PM with local $K_i = 10^{-05}$ m^2, even though their last three cylinders are filled by PM having local $K_i = 10^{-05}$ m^2 and 10^{-10} m^2, respectively.

Since PMC2 is filled with PM inter-connectors of local $K_i = 10^{-10}\,m^2$, the flow through this porous media does not encounter much transversal oscillation (see 2nd and 5th picture of Fig. 3b) for the entire range of Re tested, resulting in lesser form coefficient than that of PMC1, as listed in Table 2. However, since the flow has to squeeze through a smaller cross section (notice the flow is unable to penetrate the gaps of the cylinders because of the low permeable PM inter-connectors), the pressure-drop should now be higher for PMC2 resulting in a lower global permeability (see K_g in Table 2). Again, for PMC4, (the gaps of the first three cylinders filled by PM having local $K_i = 10^{-10}\,m^2$ and that of the last three with $K_i = 10^{-05}$ m^2), the flow structure is similar to that of PMC2 over the first three cylinders (same PM inter-connector permeability, $K_i = 10^{-10}\,m^2$), the global form coefficient, C_g, is identically lower for them, when compared to that of PMC1 and PMC3. In the case of PMC2 and PMC4, as before, it is evident that the flow structure over the last three cylinders has little effect on the global form coefficient values.

Another interesting observation from Fig. 4 is that for higher Re, the $\Delta P/L$ for PMC 1 and PMC 4 (hollow circles and '×' symbols) are less than that of the CF case (dark circular dots) because the presence of the PM inter-connector negates pressure-losses due to the originally existing recirculation in the gaps between the cylinders in the CF case. Using a non-dimensional pressure-drop defined as

$$\xi = (\Delta P/L)/(\rho U_\infty^2/2D) \tag{15}$$

these results are summarized in Fig. 5. It is clear from the plot that as $Re \to 100$, $\xi \to 1$ for all the cases, suggesting

Table 2
Global permeability (K_g) and global form coefficient (C_g) of four PMC obtained from curve-fits of Fig. 4 using Eq. (14)

Case	(K_g, m^2)	(C_g, m^{-1})
PMC 1	5.15×10^{-07}	79.02
PMC 2	3.09×10^{-07}	50.58
PMC 3	3.68×10^{-07}	80.51
PMC 4	4.00×10^{-07}	49.13

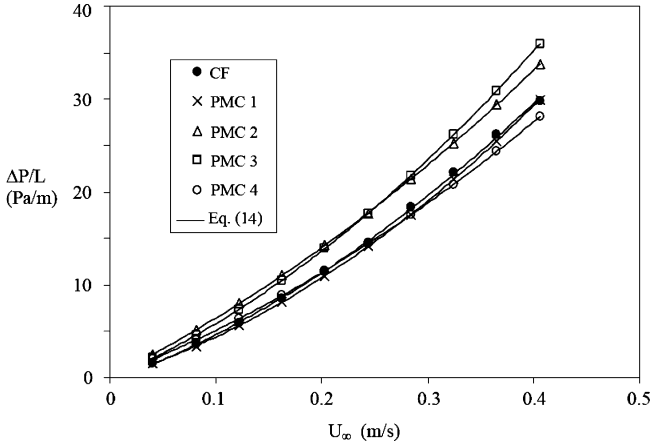

Fig. 4. Longitudinal pressure-drop variation with average velocity.

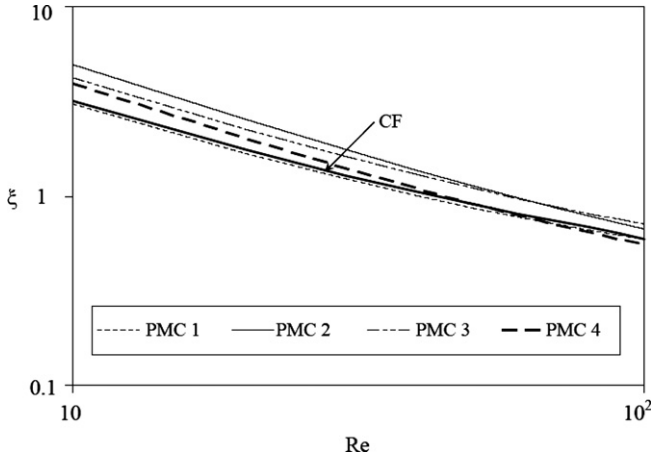

Fig. 5. Effect of K_i on ξ variation with Re.

the pressure-drop is balanced now by the quadratic drag term, i.e., the flow through the NCHX configuration perceived as a 'global' porous medium, is form drag dominated [23]. As shown in [23,25], the longitudinal pressure-drop versus average fluid speed results in Figs. 4 and 5 can be represented in the non-dimensional form

$$\xi = \frac{E}{Re} + F \tag{16}$$

where E and F capture the effects of the global viscous and form drag of the 'global' porous medium and hence includes, the variation in K_g and C_g obtained from Eq. (14). In other words, Eq. (16) can be considered as the non-dimensional equivalent of Eq. (14), with the coefficients taking, respectively, values of

$$E = 2/Da_g \quad \text{and} \quad F = 2Du_g \tag{17}$$

where, Da_g and Du_g [26], are the global non-dimensional permeability and form coefficient of the NCHX, when perceived as a 'global' porous medium, defined as

$$Da_g = K_g^{0.5}/D \quad \text{and} \quad Du_g = C_g D. \tag{18}$$

One can seek a relationship between the global Da_g and Du_g (i.e., K_g and C_g through Eq. (18)) and the rest of the NCHX parameters such as the local K_i and ϕ of the PM inter-connectors and the NCHX geometry (S_T, S_L, D) using which, the values for E and F in Eq. (17) can be evaluated. Substituting these in Eq. (16), would then yield a predictive correlation for the non-dimensional pressure-drop. For invariant heat exchanger geometry as considered in this study, the global permeability K_g in Eq. (18) is only a function of the PM inter-connector 'local' permeability (K_i, m^2). Therefore, the global Darcy number Da_g in Eq. (18) can be correlated to the PM inter-connector 'local' permeability in the following format as

$$Da_g = \frac{1}{D}\left(\frac{1}{N}\sum_{i=1}^{N}[1.07(A+B)K_i]\right)^{0.5}, \tag{19a}$$

where A and B are given as

$$A = \frac{1}{275\phi^2}\frac{S_L}{D}\left[\frac{1-(\delta/D)}{1+(\delta/D)}\right] \quad \text{and}$$
$$B = \frac{\delta}{D}\left[\frac{(H/D)-1}{1.73\phi-1}\right]^2. \tag{19b}$$

Observe in this case, $N = 6$ as the change in the K_i values between the gaps of all of the six cylinders does influence the K_g values of Table 2. In other words, since the K_i itself is changing spatially along the flow direction in the present study, Eq. (19a) utilizes a summation of the K_i effects to predict global Darcy number for all the cases (variable permeability and uniform permeability cases). For instance, while calculating K_g for PMC4 case, $K_i = 10^{-10}\,m^2$ and $10^{-5}\,m^2$ will, respectively, be used for $i = 1$–3 and 4–6 in the summation of Eq. (19a). The numerical coefficients in Eqs. (19a) and (19b) include the effect of inlet and exit penetration depth of the flow into the PM inter-connectors. The δ in Eq. (19b) represents the porous medium thickness and it is approximated for two limiting cases of PM inter-connectors, for $K_i = 10^{-10}\,m^2$ (as in PMC2 and first and last half of PMC4 and 3, respectively), δ is assumed as D, by treating the low permeable PM inter-connectors as solid. For other PM inter-connector cases of $K_i = 10^{-05}$ m^2 (as in PMC1 and first and last half of PMC3 and 4, respectively) and the CF case, δ is assumed to be 'zero', as the high permeability warrants it. The local velocity profiles in Fig. 2a through d corroborate such limiting treatment of the local permeability. The other symbols in Eq. (19), representing geometric parameters, are explained in the nomenclature.

A similar correlation is sought for the Du_g keeping in mind the fact that only the first three cylinders along with their PM inter-connectors contribute to the variation of the form coefficient, as seen in the streamlines of Fig. 3 and the pressure-drop results of Fig. 4. Hence the resulting global Du_g correlation reads

$$Du_g = D\left[\frac{1.95\phi - 0.067(\delta/D)}{(H/D) - 0.067(\delta/D)}\right]^2 \frac{1}{N}\sum_{i=1}^{3} K_i^{-0.5} \tag{20}$$

where the numerical coefficients subsume the effect of geometric parameters (S_T, S_L). The other symbols take their respective values as explained for Eq. (19) and in the nomenclature.

Combining Eqs. (19) and (20) with Eq. (17) and (18) and substituting them in Eq. (16) results in the non-dimensional pressure-drop taking the form

$$\frac{\xi}{2} = \frac{1}{0.5ReDa_g^2} + Du_g \tag{21}$$

a form similar to that used in earlier studies [23,25]. Eq. (21), together with the correlation in Eqs. (19) and (20), predicts the pressure-drop results obtained through numerical simulation within ±6% accuracy. The correlation proposed in Eq. (19) through (21) is more general than the one proposed in an earlier study [21], which was restricted to

the UP case alone and modelled the global porous medium (NCHX) using only the Darcy model.

5. Heat transfer results

Fig. 6a and b display the isotherms for $Re = 10$ and 100, respectively, in the CF case and the four PMC considered (UP and VP cases). By observing, for instance, the isotherm for $\theta = 0.95$, the similarity of the isotherms for the pairs PMC1 and PMC3 (both with $K_i = 10^{-05}$ m^2 in the first three cylinder gaps) and the PMC2 and PMC4 (both having $K_i = 10^{-10}$ m^2 in the first three cylinder gaps) are apparent. This convection effect is in line with the depth of penetration of the flow inside the PM inter-connector regions, as shown in Fig. 3a and b. Due to the penetration of the convection fluid inside the PM inter-connectors (owing to their higher permeability), it is also observed that the bulk temperature of the PMC1 and PMC3 approaches that of the wall (maximum) temperature (of the domain), even before the half way stage of the length of the NCHX. This local heat transfer enhancement even within the PM inter-connectors is not present in PMC2 and PMC4, where the local permeability is much lower (10^{-10} m^2). Nevertheless, when compared with the CF case (without the PM inter-connectors), all of these PM connected configurations enhance heat transfer from the tube wall to the convection fluid.

However, it is clear from the isotherm profiles Figs. 6a and b that since the fluid above the PM inter-connector region reaches about 80% of the maximum (wall) temperature of the domain within first three cylinders of the NCHX configuration itself, irrespective of the permeability of the PM inter-connectors, connecting the last three cylinders with the PM-inter-connectors (of such permeability values) does not help much in the local heat transfer enhancement of the last three cylinders. This situation is explained well in the temperature profiles of Fig. 7. In Fig. 7(a,b) and (c,d), drawn, respectively, for $Re = 10$ and 100, at the mid-section and exit of the NCHX configuration. Even though the temperature profiles at the mid-section for PMC1–4 are distinct and different from that of the CF in the region above the PM inter-connectors, they all are almost identical inside the PM inter-connector region. The presence of the PM inter-connectors contributes more to the additional pressure-drop penalty across the NCHX.

The overall heat transfer coefficient for NCHX is calculated using the temperature at the exit and inlet, the Nu is defined as

$$Nu = qD/A(T_w - T_{bn})k_f N, \tag{22}$$

where all the parameters are explained in the nomenclature. The overall heat transfer coefficient Nu variation with Re is shown in Fig. 8, for all the PM cases, listed in Table 1. It can be observed from Fig. 8 that apart from the usual Re dependence, the Nu also increases with the increase in the Du_g, when the NCHX configuration is viewed as a porous media. From Eq. (20), the increase in Du_g can be seen as the effect of the increase in K_i, the local permeability. The

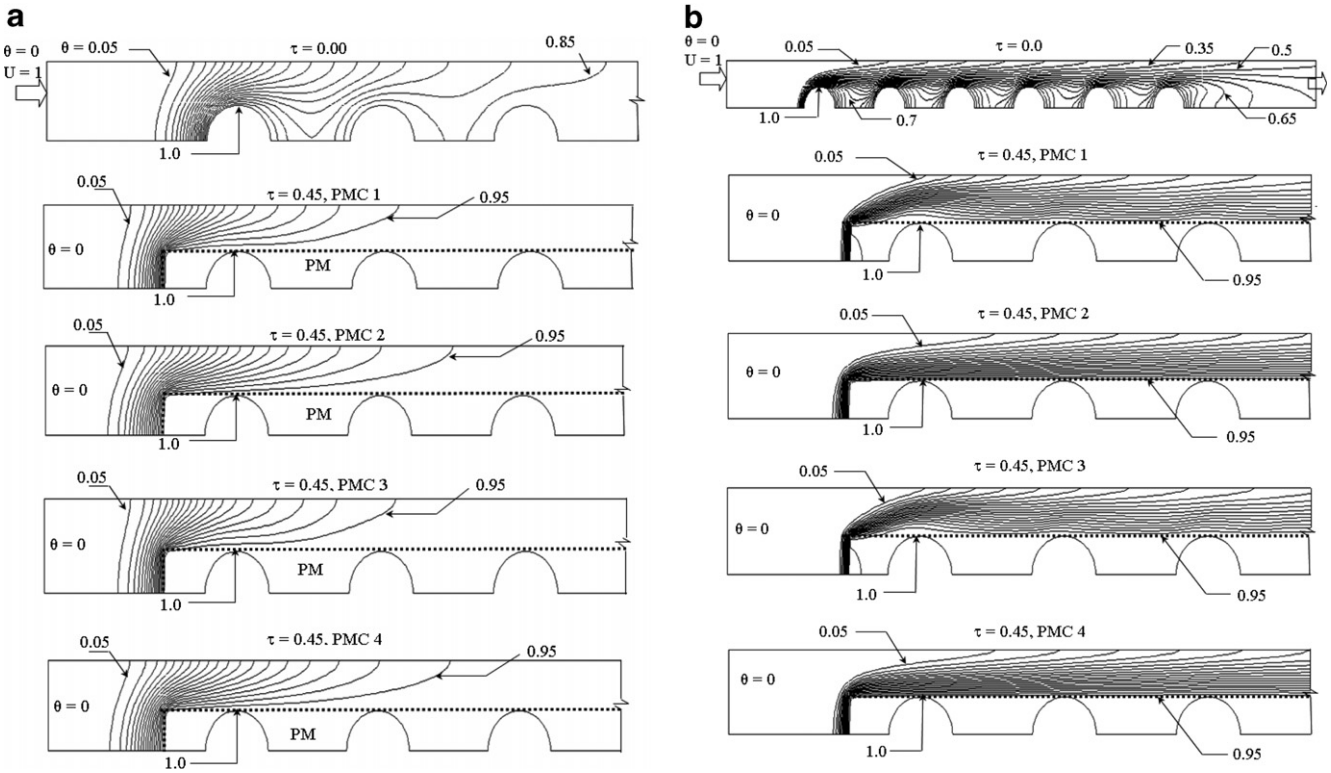

Fig. 6. Isotherms for the CF and PM configuration listed in Table 1 at Re = (a) 10 and (b) 100.

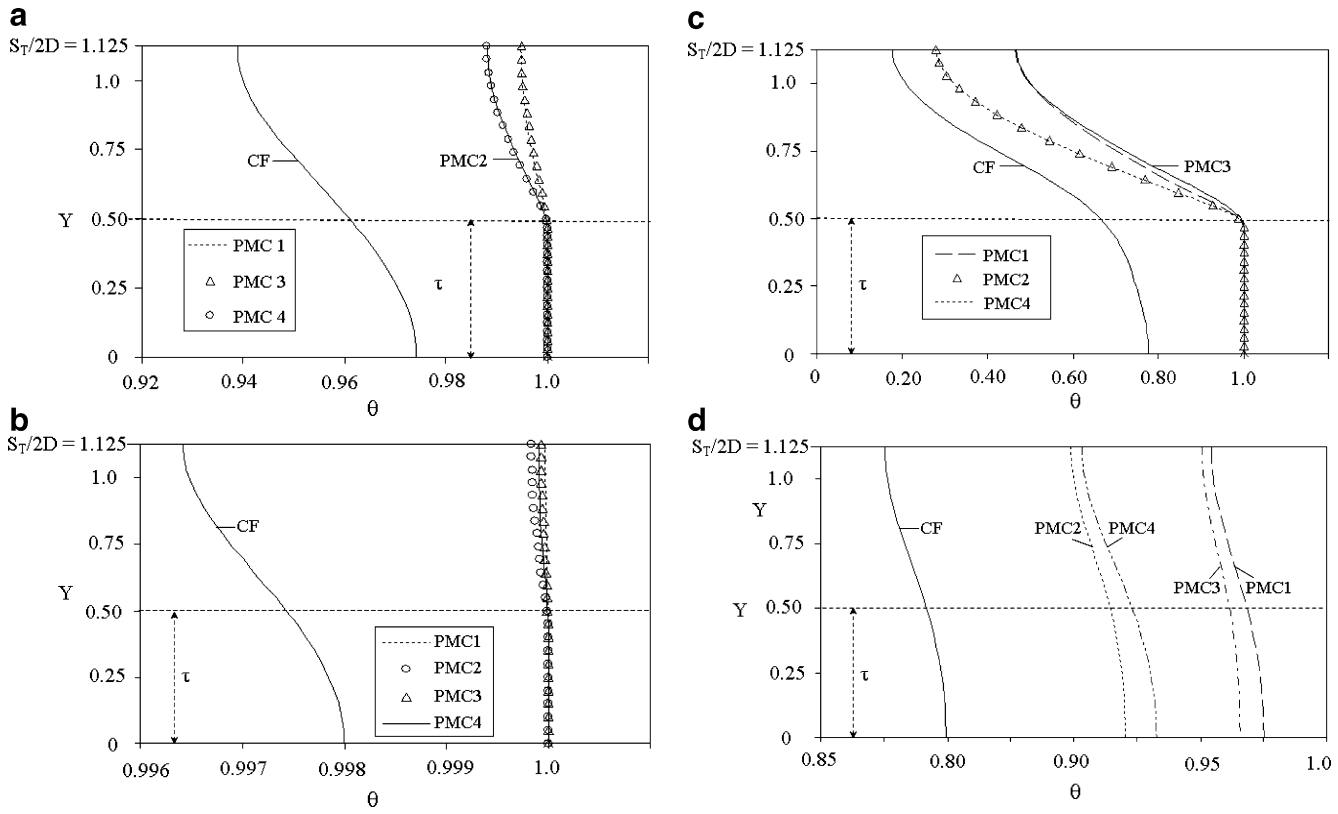

Fig. 7. Local dimensionless temperature profiles for $Re = 10$ (a) mid-section (b) exit and for $Re = 100$ at (c) mid-section (d) exit of the configuration.

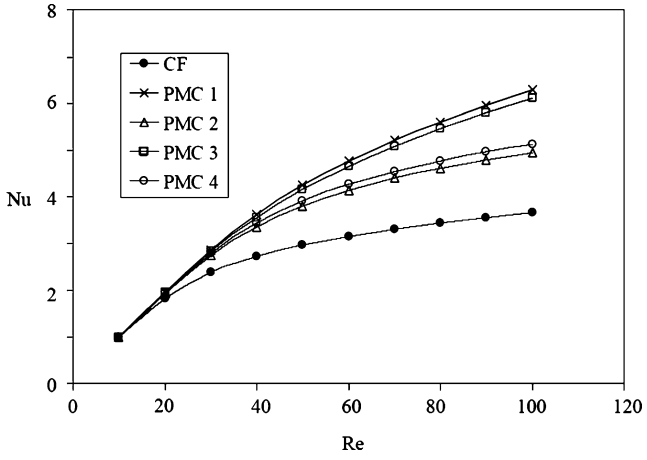

Fig. 8. Effect of K_i on Nu versus Re.

earlier plot of Fig. 7d registered maximum exit temperature for the UP case of PMC1, resulting in the lowest temperature difference ($T_w - T_{bn}$). The average heat flux q/A from all of the tubes also increases for increase in T_{bn}, resulting in a maximum Nu, Eq. (22). Although for the VP cases of PMC3 and PMC4, Nu curves fall in between the two limiting values for PM cases of PMC1 and PMC2, the Nu value of PMC3 is higher than that of PMC4 due to the fact that the Du_g for PMC3 is higher, leading to stronger forced convection within the first three cylinders of the NCHX configuration.

Comparing PMC1 and PMC3, their PM inter-connectors in the first three cylinders have identical permeability values, allowing similar strong forced convection situation (as supported by the isotherms in Fig. 6). The mild drop in Nu values of PMC3 from that of PMC1 is because of the inability of the convection fluid to enter the PM inter-connector in the last three cylinders of PMC3. For PMC4, the local permeability is lowest in the beginning three cylinders disallowing more fluid through the PM inter-connector, thus preventing strong forced convection (although convection is still present) when the temperature difference between the tube (maximum) and the convection fluid is large. This results in a significantly lower Nu value for PMC4 than that of PMC3 (both VP cases) and much closer to the PMC2, UP case.

For the chosen NCHX configuration (Fig. 1) with the PM inter-connectors (Table 1) made of aluminium metal foam having $k_s = 202$ W/m K, the overall Nu in Fig. 8 is correlated with Re and Du_g, Eq. (20), as

$$Nu = 0.16Re^{0.73} + 1.5Du_g^{0.2}; \quad 20 < Re < 100. \tag{23}$$

Eq. (23) predicts an increase in the overall Nu as Re increases irrespective of the inter-connector PM configuration. The effect of PM inter-connector is subsumed in the Du_g values (see Eq. (20)). The above correlation Eq. (23) predicts the overall Nu data obtained using numerical simulations (Fig. 8), within ±6% accuracy. For $Re = 10$ and 20 (in Fig. 8), it predicts the Nu values within ±20% accuracy.

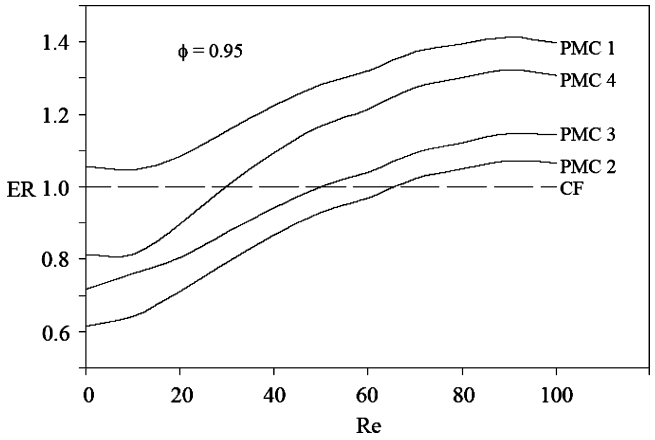

Fig. 9. ER versus *Re* for CF and PM configuration listed in Table 1.

Unlike the partial PM configuration of [14], the present partly PM filled NCHX situation exhibits strong form-drag dependence (Du_g) of *Nu*, even for $Da_g \sim 10^{-1}$ (predicted using Eq. (19)), under laminar flow.

6. Overall enhancement ratio

A comparison of the pressure-drop penalty incurred and the heat transfer enhancement achieved for the PM inter-connector models is expressed using overall energy gain [24] of the system as

$$R = (Q_f/\mathrm{UA_C}\Delta P) \tag{24}$$

where Q_f is the heat carried by the fluid $(=\dot{m}c_p(\overline{T}_{b-exit} - \overline{T}_{in}))$, U is the average velocity through the duct, A_c is the area of the cross section and ΔP is the pressure-drop across the tube bank. The overall enhancement ratio (ER) of the system can be defined using the overall energy gain of the system with PM and without PM case as

$$\mathrm{ER} = R_{PM}/R_{CF}. \tag{25}$$

Fig. 9 shows the variation of ER with *Re* for all of the PMC listed in Table 1. It can be observed for all of the PMC that the variation of ER increases with *Re* and starts decreasing at $Re = 90$. At higher flow rates the magnitude of the non-linear drag term in Eq. (14) becomes significant, leading to an increased overall pressure-drop resulting in a decrease in ER, Eq. (25), even for similar behaviour of *Nu* values with respect to *Re*. It is clear from Fig. 9 that higher ER values are registered for the PM inter-connectors of higher permeability case, PMC1. Similarly, because of the highest *Nu* values (Fig. 8) and the reduced pressure-drop even when compared with the CF case (Fig. 4), PMC1 results in the maximum ER values within the *Re* tested range.

7. Conclusions

Using detailed numerical simulations, it is shown in this paper that tube-to-tube PM inter-connectors can enhance the heat transfer from the tubes to the cooling fluid, in a typical near compact heat exchanger (NCHX) configuration. The PM inter-connectors are made of metal foam with permeability ranging between 10^{-5} and $10^{-10}\,m^2$, and are placed in the longitudinal direction, between the six successive tubes considered in in-line arrangement. The parameters used for analysing the results are the global non-dimensional pressure-drop (ξ) and heat transfer coefficient (*Nu*) for the NCHX with and without local PM inter-connectors of uniform permeability (UP, PMC1 and PMC2, see Table 1) and variable permeability (VP, PMC3 and PMC4, see Table 1).

Treating the NCHX as a 'global' porous medium, it is shown in this paper that their overall enhancement ratio (heat transfer coefficient, *Nu*, and non-dimensional pressure-drop, ξ) is being influenced by the presence of 'local' tube-to-tube porous medium (PM) inter-connectors.

Further, in the six cylinder NCHX configuration tested, the effect of the flow structure over the last three cylinders seems not to affect the form drag component at all, as seen from the identical C_g results for PMC1 and PMC3, both having the first three cylinders filled by PM with local $K_i = 10^{-05}\ m^2$, even though their last three cylinders are filled by PM having local $K_i = 10^{-05}\ m^2$ and $10^{-10}\,m^2$, respectively.

For the UP cases (PMC1 and PMC2, see Table 1), the overall NCHX *Nu* was found to be directly proportional to the increase in the local interconnecting PM permeability K_i, for all the *Re* tested. This is seen in the higher values of *Nu* of PMC1 ($K_i = 10^{-5}\,m^2$) than that of PMC2 ($K_i = 10^{-10}\,m^2$).

By modifying the local cooling flow in such inter-connectors using PM with suitably varying permeability, it is shown that one can control the heat transfer from successive tubes in such NCHX configuration. This is corroborated by the results of *Nu* variation with *Re* for the VP case of PMC3 and PMC4, which fall very close to the UP cases of PMC1 and PMC2, respectively. The *Nu* variation for *Re* for VP cases (PMC3 and PMC4) is bounded by the two limiting UP cases PMC1 and PMC2 as expected, for identical porosity.

Comparisons between NCHX tube bank in the UP and VP cases with the no-porous medium inter-connector case (CF) are done using an overall enhancement ratio (ER) defined as the ratio between the heat transfer and the pumping power ratio incurred for the PM case over the CF case. At higher flow rates ($Re > 70$) it is shown that the VP case of PMC4 registers less pressure-drop compared to PMC1, the UP case with highest K_i. Hence, the overall enhancement ratio ER is seen to improve by using a variable permeability PM tube-to-tube inter-connectors over the uniform permeability PM inter-connectors.

By treating the NCHX as a 'global' porous medium, separate useful engineering correlations predicting ξ and *Nu* as a function of *Re*, Da_g and Du_g (the last two are, in turn, correlated to Da_i) have been developed. Both correlations predict the numerical data with ±6% accuracy.

References

[1] G. Lauriat, R. Ghafir, Forced Convective Heat Transfer in Porous Media, in: K. Vafai (Ed.), Handbook of Porous Media, Marcel-Dekker, New York, 2000, pp. 201–268.

[2] A. Bejan, I. Dincer, S. Lorente, A.F. Miguel, A.H. Reis, Porous and Complex Flow Structures in Modern Technologies, Springer-Verlag, New York, 2004.

[3] P.-X. Jiang, M. Li, T.-J. Lu, L. Yu, Z.-P. Ren, Experimental research on convection heat transfer in sintered porous plate channels, Int. J. Heat Mass Transfer 47 (2004) 2085–2096.

[4] D.A. Nield, A.V. Kuznetsov, Transverse heterogeneity effects and thermal development, in: K. Vafai (Ed.), Handbook of Porous Media, second ed., Taylor & Francis pub, New York, 2005, pp. 144–194.

[5] J.L. Lage, A. Narasimhan, D.C. Porneala, D.C. Price, Experimental study of forced convection through micro porous enhanced heat sinks, in: D.B. Ingham et al. (Eds.), Emerging Technologies and Techniques in Porous Media, Kluwer Acad. Pub, Netherlands, 2004, pp. 433–452.

[6] J.L. Lage, A.K. Weinert, D.C. Price, R.M. Weber, Numerical study of low permeability micro-porous heat sink for cooling phased-array Radar systems, Int. J. Heat Mass Transfer 39 (1996) 3622–3647.

[7] J.L. Lage, D.C. Price, R.M. Weber, G.J. Schwartz, J. McDaniel, Improved cold plate design for thermal management of phased array Radar systems, US Patent Office Patent #5960861, 1999.

[8] J.L. Lage, A. Narasimhan, Porous media enhanced forced convection: fundamentals and applications, in: K. Vafai (Ed.), Handbook of Porous Media, Marcel-Dekker, New York, 2000, pp. 357–394.

[9] A. Hadim, Forced convection in a porous channel with localized heat sources, ASME J. Heat Transfer 116 (1994) 465–472.

[10] C. Cui, X.Y. Huang, C.Y. Liu, Forced convection in a porous channel with discrete heat sources, ASME J. Heat Transfer 123 (2001) 404–407.

[11] D.C. Chandrasekhara, P.M.S. Namboodiri, Influence of variable permeability on combined free and forced convection about inclined surfaces in porous media, Int. J. Heat Mass Transfer 28 (1985) 199–206.

[12] N.J. Rabadi, E.M. Hamdan, Free convection from inclined permeable walls embedded in variable permeability porous media with lateral mass flux, J. Petrol. Sci. Eng. 26 (2000) 241–251.

[13] I.P. Bogdan, A.A. Mohamad, An experimental and numerical study on heat transfer enhancement for gas heat exchanger fitted with porous media, Int. J. Heat Mass Transfer 47 (2004) 4939–4952.

[14] A.A. Mohamad, Heat transfer enhancements in heat exchangers fitted with porous media Part I: constant wall temperature, Int. J. Ther. Sci. 42 (2003) 385–395.

[15] T.V. Morosuk, Entropy generation in a conduits filled with porous medium totally and partially, Int. J. Heat Mass Transfer 48 (2005) 2548–2560.

[16] A.V. Kuznestov, Analytical studies of forced convection in partly porous configuration, in: K. Vafai (Ed.), Handbook of Porous Media, Marcel Dekker, New York, 2000, pp. 269–312.

[17] S.V. Patankar, C.H. Liu, E.M. Sparrow, Fully developed flow and heat transfer in duct having stream-wise periodic variation of cross-sectional area, ASME J. Heat Transfer 99 (1977) 180–186.

[18] J.A. Ochoa-Tapia, S. Whitaker, Momentum transfer at the boundary between a porous medium and a homogeneous fluid – I, theoretical development, Int. J. Heat Mass Transfer 38 (1995) 2635–2646.

[19] B. Alazmi, K. Vafai, Analysis of fluid flow and heat transfer interfacial conditions between a porous medium and a fluid layer, Int. J. Heat Mass Transfer 44 (2001) 1735–1749.

[20] S.V. Patankar, Numerical Heat Transfer and Fluid Flow, Taylor & Francis, 1980.

[21] K.S. Raju, A. Narasimhan, Porous medium approach to study thermo-hydraulics of near compact heat exchangers treated as porous media, ASME J. Heat Transfer 129 (2007) 273–281.

[22] A. Narasimhan, K.D. Sahu, Heat transfer augmentation in a near compact heat exchanger using porous medium fins, in: 18th National and 7th ISHMT–ASME Heat Mass Transfer Conference, 2006, pp. 115–1121.

[23] L. Wilson, A. Narasimhan, S.P. Venkateshan, Turbulent flow hydrodynamic experiments in near-compact heat exchanger models with aligned tubes, ASME J. Fluids Eng. 126 (2004) 990–996.

[24] J.L. Lage, B.V. Antohe, Darcy's experiments and the deviation to nonlinear flow regime, ASME J. Fluids Eng. 122 (2000) 619–625.

[25] A.A. Zukauskas, Convective heat transfer in cross flow (Chapter 6), in: S. Kakac, R.K. Shah, W. Aung (Eds.), Hand Book of Single Phase Convective Heat Transfer, Wiley, NY, 1987.

[26] J.L. Lage, P.S. Krueger, A. Narasimhan, Protocol for measuring permeability and form coefficient of porous media, Phys. Fluids 17 (8) (2005) 1–4, Paper No.088101.